Nanoscale

Nano-Chevron Quantum Dot for All Electrical Spin-Qubit Applications

Journal:	*Nanoscale*
Manuscript ID	NR-ART-05-2021-002842.R1
Article Type:	Paper
Date Submitted by the Author:	08-Jul-2021
Complete List of Authors:	Tiessen, John; University of Illinois at Chicago College of Engineering Shi, Junxia; University of Illinois at Chicago, Electrical and Computer Engineering

SCHOLARONE™
Manuscripts

Please do not adjust margins

ARTICLE

Received 4th May 2021,
Accepted 00th January 20xx

DOI: 10.1039/x0xx00000x

Nano-Chevron Quantum Dot for Spin-Qubit Applications

John Tiessen[a] and Junxia Shi[a†]

We study the theoretical properties of a parabolic hBN/MoS_2/hBN heterostructure quantum dot potential generated via electrostatic gates and its interaction with a Cobalt nano chevron. We demonstrate that such an example system can undergo electric dipole spin resonance for a single electron isolated to the K' valley within the MoS_2 monolayer, and such a system can achieve pi-rotation times of approximately 5.5 ns under the influence of a 20.89 GHz driving field. Our proposed system requires operating conditions easily achievable with current experimental methods and would allow for the all-electrical control of a spin-qubit within an MoS_2 device. Our results show that such a system is experimentally feasible and would have comparable properties to that of more traditional silicon based spin-qubits. Furthermore, the design of the device can be applied to other material systems beyond MoS_2 and Cobalt. In theory, the proposed structure could make use of any 2D material that experiences strong proximity exchange interactions with other magnetic materials, which makes our proposed design highly general.

Introduction

One of the main problems related to scaling silicon quantum dot (QD) designs is that they often require a laterally varying magnetic field.[1-4] This creates a position-dependent Zeeman splitting required to couple the spin qubit to an alternating electric field, which in turn is used for qubit manipulation and operation in electric dipole spin resonance (EDSR).[2] The generation of the positionally varying magnetic field is accomplished via the deposition of micromagnets, which generate the desired magnetic field.[3-5] However, the scalability is inherently limited and the design faces several obstacles, according to studies related to foundry fabricated silicon QDs.[6] Therefore, finding an alternative way to generate the positionally dependent Zeeman splitting would greatly simplify the design of semiconductor based QDs and would be most desirable.

Another issue with semiconductor-based qubits and QDs is that they need to be highly tunable. Due to the inherent variability of semiconductor production, being able to tune the relevant properties of thousands of qubits individually through all electrical means is critical. Currently, this is achieved by finding the right spot between micromagnets where the inhomogeneous magnetic field is of the correct form to allow for EDSR.[4]

To get around some of these problems, we propose an MoS_2 spin-qubit making use of the proximity exchange interaction to achieve a highly tunable spin-qubit, whose position can be well known and whose properties can be tuned using all electric means in multiple ways. Based on the way this quantum dot is constructed, we will refer to it as a nano-chevron quantum dot (NC-QD). Such a quantum dot is inherently more scalable and has unique advantages when compared to other semiconductor based QD designs.

Results and discussion

Quantum Dot Qubit Setup

The proposed qubit makes use of the proximity exchange interaction to control the spin-splitting within the K'-valley of the conduction band of MoS_2. The proximity exchange interaction has been an active area of research over the last few years, with researchers using various proximity interactions mainly to study and manipulate the properties of two-dimensional materials.[7] Due to the atomic scale thickness of 2D materials, proximity interactions can have a strong effect on the electronic properties of 2D materials when paired with an appropriate magnetic material. The effects of proximity interactions on 2D materials have been demonstrated in detailed numerical calculations[8-13] as well as experiments.[14-17] In this study, we employ TMDC/magnet heterostructures and take advantage of the magnetic proximity exchange interaction between them to design qubits. In these TMDC/magnet heterostructures, the TMDC layer acts as if it is under the influence of a magnetic field of

[a] *Department of Electrical and Computer Engineering, University of Illinois at Chicago, Chicago, IL 60607.*
† Corresponding author: lucyshi@uic.edu
Electronic Supplementary Information (ESI) available: [details of any supplementary information available should be included here]. See DOI: 10.1039/x0xx00000x

Please do not adjust margins

approximately 10 Tesla,[18] although the magnetic field in these structures is directly measured to be less than 1 Tesla.[19]

It is precisely this interaction that we aim to take advantage of in our device design. Due to the short-range of proximity exchange interactions,[6] patterning an appropriate magnetic material on top of a TMDC can be used to introduce a symmetry breaking perturbation. This in turn can be used to create spatial separation between the spin-up and spin-down wavefunctions, analogous to what has been done with slanting Zeeman potentials, and can therefore allow for EDSR.[2, 3, 20]

Our proposed system consists of a heterostructure with a monolayer of MoS_2 which is sandwiched by monolayers of hBN, on top of which a ferromagnetic (FM) Cobalt (Co) nano-chevron (NC) is placed. The ferromagnet is not limited to Co, as will be discussed later. The band structure of the MoS_2 directly below the Co is shifted via proximity exchange interactions.[9] Due to the short-range of the proximity exchange interaction, we approximate this as a step-function shift in the energies of the spin-up and spin-down electrons in the MoS_2 conduction band, which is entirely position dependent. In other words, electrons in the MoS_2 layer located under the Co chevron experience a higher or lower potential than electrons in the MoS_2 layer without the Co NC overhead, depending on the spin of the electron. The general concept behind the NC quantum dot is visualized in Figure 1(a) and 1(b).

It is important to note that even though other magnetic materials can be used to achieve the same design goals, we focus on the use of Co as the ferromagnet in this work, as the interaction between Co and MoS_2 has been modeled as a separate term in the Hamiltonian from that of a bare MoS_2/hBN system,[9] and the relative energy of the spin-up and spin-down electrons in the presence and absence of the FM NC can be determined. Many other ferromagnetic materials could be used. However, Co will suffice to demonstrate the principles of our qubit. In this work, we assume that the NC is extremely thin and that the tunneling time for electrons to move from the MoS_2 layer into the NC is longer than the spin rotation time. Also, we assume that due to the extreme thinness of the Co layer used in the DFT calculations[9,11] and the unusual shape of the NC, very few free electrons will be able to reside within the NC itself. Furthermore, we assume that the NC does not interact strongly with the time-dependent electric field used for EDSR. In general, perturbation theory can be used to estimate the suitability of a given FM material, provided that the relative energies of the spin-up and spin-down electrons for the proximitized and bare TMDC are well known.

Next, a series of electrostatic gates are placed around this NC along with a suitable back-gate potential to form a parabolic electrostatic potential. To prevent tunneling from the back gate to the MoS_2, a sufficiently thick SiO_2 layer is present in between. Detailed theoretical calculations have shown that the electrostatic potentials formed by gates on 2D materials are parabolic in nature.[21,22] Therefore, we treat the Co NC as a position-dependent step-function which either raises or lowers the energy of spin-down and spin-up electrons, depending on their position within the confining potential. The energy shift of the spin-up and spin-down electrons is calculated based on the low energy effective Hamiltonian (LEH), [9] and the values are summarized in Table 1.

The K and K' valleys are inequivalent conduction band minimums in the momentum space, which are normally degenerate in energy in the absence of an external field. Although degenerate in energy, they are inequivalent in terms of spin. In this case, the ground state of the K' valley is spin-down while the ground-state of the K valley is spin-up.[9,11] In this work, we primarily focus on the K'-valley, as it is the K'-valley that has the spin ordering reversed, therefore the energies of spin-up and spin-down electrons are raised at different rates, when an applied external magnetic field magnetically aligns the NC in the $+\hat{\boldsymbol{z}}$ direction. This in turn allows for the spin-up and spin-down energies to be brought closer together in energy, which is useful for EDSR.

STATE	MoS_2/hBN (meV)	MoS_2/hBN/Co (meV)	MASS (m/m_e)
$\|\boldsymbol{K}',\uparrow\rangle$	879.361	877.664	0.49
$\|\boldsymbol{K}',\downarrow\rangle$	876.639	878.336	0.44
$\|\boldsymbol{K},\uparrow\rangle$	876.639	874.942	0.44
$\|\boldsymbol{K},\downarrow\rangle$	879.361	881.058	0.49

Table 1. Energies of the spin states in the *K* and *K'* valleys calculated based on the LEH, [9] which are used for determining the energies of $|K',\uparrow\rangle$, $|K',\downarrow\rangle$, $|K,\uparrow\rangle$ and $|K,\downarrow\rangle$ states in the TMDC/hBN/FM heterostructures, and the spin-up and spin-down effective mass from DFT calculations.[23]

(a)

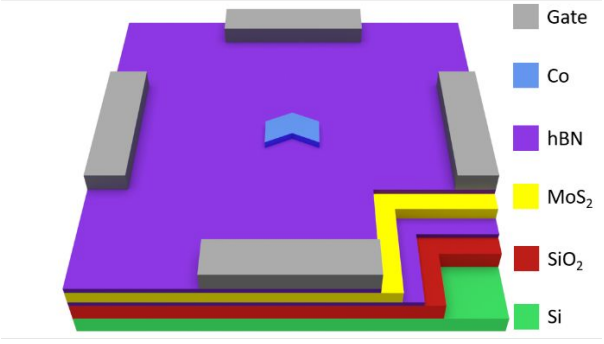

(b)

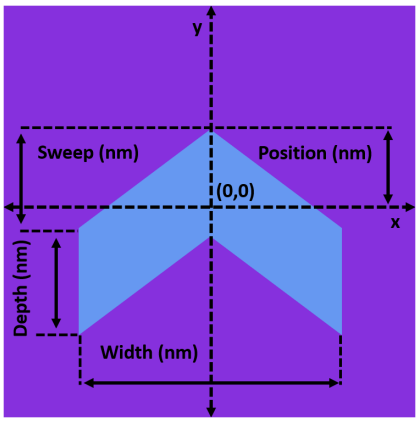

This journal is © The Royal Society of Chemistry 20xx

Fig. 1. (a) A general layout of the proposed device with purple indicating monolayer (ML) hBN, yellow ML MoS_2, blue Co (or any other proximity exchange material), red SiO_2 insulating layer, and green the substrate. The grey blocks represent the electrostatic gates, which form the parabolic potential. (b) A closeup of the Co chevron with geometric elements relevant to the proposed device: sweep (the slope of the chevron's legs), position relative to the origin defined at $x = 0$, width in the x-direction, and depth of the chevron in the y-direction. These properties are defined mathematically in equation 1b.

Since the electrostatic potential is parabolic and the energy of each state relative to the bottom of the well is of interest, the relative energies of these states are used in the calculations, with 0 meV referring to the lowest energy state of the four. Table 2 shows these relative energies, which are measured from the spin-up/spin-down conduction band minimum (CBM) energies of spin-down and spin-up electrons within the K' valley are shown in Figures 2(a) and 2(b) respectively. The Hamiltonian of the NC-QD is described by Equation 1 below.

In Equation 1a, the first term is a Landau term taking into account the interaction of the electron with the perpendicular magnetic field,

$$H = H_B + \frac{V_{max}}{R_{QD}^2}(x^2 + y^2) + \alpha_{\tau,s} + \frac{1+\tau}{2}\hbar\left(\frac{e^-|B_z|}{m_{\tau,s}}\right) + \frac{1}{2}\left(\tau g_{vl} + g_{sp}^{\perp} s\right) B_z g_{sp}^{\perp} \mu_B - sV_{NC}(x,y) \qquad (1a)$$

$$V_{NC}(x,y) = \begin{cases} \gamma, & if \;\; y < -m|x| + b \; and \; y \geq -m|x| + (b-a) \; and \; |x| < c \\ 0, & Otherwise \end{cases} \qquad (1b)$$

$$H_B = i\hbar\frac{e^- B_z}{2m_{\tau,s}}\left[y\frac{\partial}{\partial x} - x\frac{\partial}{\partial y}\right] + \frac{m_{\tau,s}}{2}\left(\frac{e^{-2}B_z^2}{4m_{\tau,s}^2}\right)(x^2 + y^2) \qquad (1c)$$

assuming that the entire system is either MoS_2/hBN or MoS_2/hBN/Co.

STATE	MoS_2/hBN (meV)	MoS_2/hBN/Co (meV)	MASS (m/m_e)
$\|K',\uparrow\rangle$	3.0	1.0	0.49
$\|K',\downarrow\rangle$	0.0	2.0	0.44
$\|K,\uparrow\rangle$	0.0	−2.0	0.44
$\|K,\downarrow\rangle$	3.0	4.0	0.49

Table 2. The relative energy of the spin-up and spin-down states in the presence and absence of the Co proximity exchange interaction. All energies are measured relative to the lowest energy in Table 1, which is the ground state of the proposed qubit.

Next, the effect of the magnetic NC on the wavefunctions of the spin-up and spin-down electrons, which are confined to the QD potential, is considered. Intuitively, a wavefunction spends less time where its probability density is lower. Therefore, if we assume that the wavefunction were centered near the tip of the NC then the effect of the Co NC would be felt most strongly near the minimum of the well and would rapidly diminish towards the edges. However, since the NC is not symmetric along the x-axis, it generates on average a variable Zeeman splitting in the y-direction. This is because the electron will spend less time further away from the minimum and the legs of the NC are slanting away from the center. This is how an effective slanting Zeeman field is created with the position-dependent interaction with the NC. The asymmetry of the NC along the x-axis is important to the ability of the proposed QD to couple the spin-up and spin-down states to an alternating electric field, which will be discussed later.

For a parabolic potential with a ferromagnetic NC perturbation of a depth of 300 meV,[24] and a radius of 40 nm, based on the proposed QD radius (R_{QD}) in reference 23, the potential which is further described in equation 1c. In equation 1c we have taken into account the effect of the magnetic field on the electron via a vector potential that has been implemented in the symmetric gauge.[25] The second term is the well-known parabolic well potential adapted from reference 24. $\boldsymbol{V_{max}}$ is the depth of the quantum well (300 meV), $\boldsymbol{R_{QD}}$ is the QD radius (40 nm), $\boldsymbol{x}$ and $\boldsymbol{y}$ are the cartesian position coordinates and are measured in nanometers. In our model, $\boldsymbol{\alpha_{\tau,s}}$ is the energy of the electron at the conduction band minimum for a given spin and valley, where $\boldsymbol{\tau} = \pm\,\mathbf{1}$ for the *K'* (*K*) valley and $\boldsymbol{s} = \pm\,\mathbf{1}$ for spin-up (down). The value of $\boldsymbol{\alpha_{\tau,s}}$ can be read off from Table 2. In a similar way $\boldsymbol{m_{\tau,s}}$ can also be read off from Table 2. The spin-up energy is determined by choosing $\boldsymbol{s = +1}$ while the spin-down energy is determined by selecting $\boldsymbol{s = -1}$. The terms $\boldsymbol{g_{vl}}$ and $\boldsymbol{g_{sp}}$ are the effective valley and spin g-factors with values of 0.75 and 1.98 respectively for MoS_2.[23] Equation 1b describes the perturbing potential created by the magnetic NC. For Co, the proximity exchange interaction raises or lowers the energy of the spin-down and spin-up electrons, respectively, by $\boldsymbol{\gamma}$ where $\boldsymbol{\gamma = 2.0}$ meV. a, b, and c are the dimensions of the NC with 'a' being the 'depth' of the NC in the y-direction (9 nm), 'b' is the NC tip position (7 nm) and 'c' half the NC width (10 nm). The slope/sweep of the NC in our studied structure 'm' is set to 1.

Figure 2 shows the potential experienced by the spin-down and spin-up electrons within the K'-valley of the Co nano-chevron QD. Notice that the shape of the NC is clearly visible. It is also observed that the Co chevron creates either a depression or a rise in the potential, depending on the spin of the electron. Due to the parabolic shape of the confining potential, the Co NC affects the electron strongly near the center of the potential and becomes less relevant as the electron moves further away. The behavior of the QD as a function of NC position is discussed next.

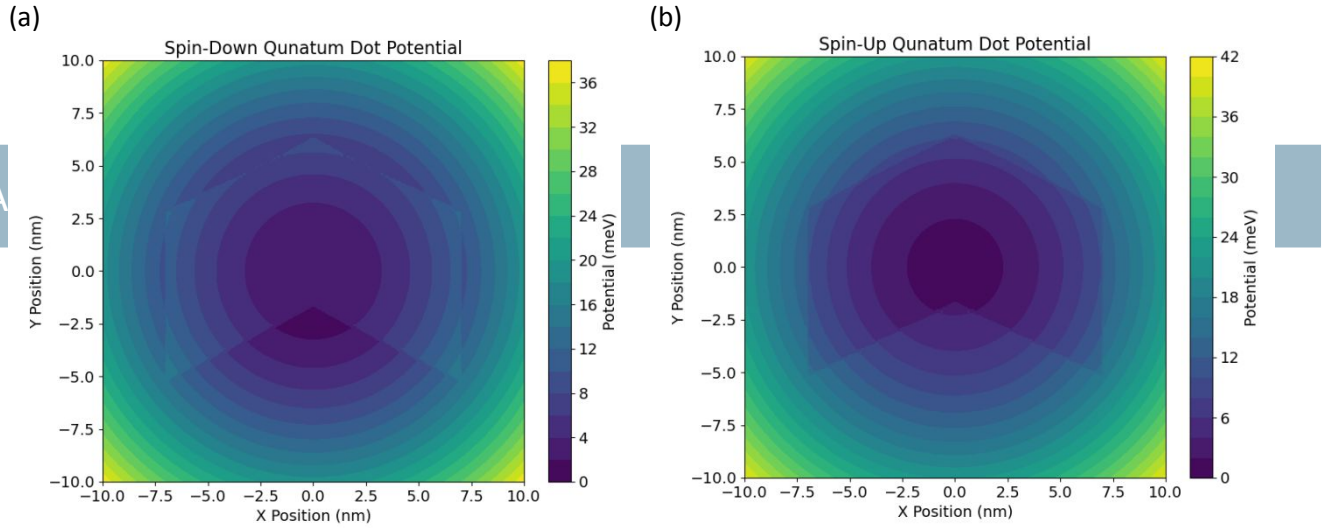

Fig. 2. (a) The quantum dot potential experienced by the spin-down electron within the K'-valley of the NC QD. (b) The quantum dot potential experienced by the spin-up electron within the same system. Note that both potentials assume an initial parabolic potential of a depth of 300 meV and a QD radius of 40 nm and the NC is treated like a position-dependent perturbing step-function.

NC Position vs. Spin-Up and Spin-Down Energy

The position of the ferromagnetic NC relative to the center of the parabolic potential has a large effect on the spin splitting between the spin-up and spin-down states. In this work, we carry out several different calculations with different NC parameters (width, sweep) to determine the optimal shape for enhancing EDSR. The optimization procedure involves iterating through different NC parameters and the consequential NC-QD properties. Of primary interest is how stable the energy separation is between the spin-up and spin-down states at the optimum NC position as well as the overlap between the spin-up and spin-down wavefunctions. To determine the energy of the spin-up and spin-down states in the NC parabolic potential, we solve the 2D Schrödinger Equation using the Direct Matrix Method,[26] where the eigenvalues and eigenvectors of the matrix are found using the built-in SciPy eigenvalue/eigenvector solver.[27] To incorporate the effect of applied external magnetic field in the z-direction, the symmetric vector potential from eqn (1c) needs to be incorporated into the resulting numerical matrix, for which we use the so-called 'naïve' discretization method.[28] It should be noted that this method is reasonably accurate as the perpendicular magnetic field is represented in the symmetric gauge,[29] which should not introduce any significant errors.

Due to the complex nature of the numerical methods used to calculate the energy of the spin-up and spin-down ground states within the K'-valley, the number of samples that can be taken of the potential space is limited. In Fig. 3(a), we use 128^2 samples of the 2D potential to calculate the spin-up and spin-down energy versus the position of the NC. 128^2 samples are also used along with the optimized NC position to determine the effect of the applied external magnetic field on the energy of the different possible valley-spin states. This should offer a sufficient resolution to achieve high accuracy of the spin-up and spin-down ground states. In order to increase the resolution of the calculations without increasing the number of samples in the potential space, the NC-QD potential needs only to be simulated out to a radius of 20 nm rather than the full 40 nm. Appendix A further explains in detail why this is an appropriate approximation. To summarize, the ground states of the NC-QD are almost completely contained within the first 20nm of the potential. In fact, wavefunctions up to the third excited state should be well approximated within a radius 20nm from the center of the NC-QD potential. Beyond a radius of 20 nm, the potential is treated as infinite.[26] Using a ±20 nm simulation limit in the x and y directions, it is possible to obtain a resolution of approximately 0.098 nm^2 per sample of the NC-QD potential.

Figure 3(a) shows the calculated energies of the lowest spin-up and spin-down states as a function of the Co NC position in y-direction relative to the center of the parabolic potential. After fitting the data in Fig. 3(a) with quadratic equations, the point at which the spin-up and spin-down states come the closest in energy is determined to be at the NC tip position of approximately 7 nm. It is also worth noting here that the spin-up and spin-down energies have a parabolic-like behavior near the minimum energy difference. This is a desirable property for a QD system, as the energy versus position behavior is effectively flat near the minimum energy difference point. When an alternating electric field is applied to the system, it will not change the energy splitting significantly, therefore allowing a simpler application of EDSR.

To determine the relationship between the applied external magnetic field and the energy of the $|\boldsymbol{K}',\uparrow\rangle$, $|\boldsymbol{K}',\downarrow\rangle$, $|\boldsymbol{K},\uparrow\rangle$ and $|\boldsymbol{K},\downarrow\rangle$ states, a series of numerical calculations are required. Fig. 3(b) shows the energies of the different spin-valley states calculated via equation 1(a) with varying magnetic field, as well as linear lines fitting the numerical results. This allows us to estimate the required magnetic field in order to bring the $|\boldsymbol{K}',\uparrow\rangle$ and $|\boldsymbol{K}',\downarrow\rangle$ states close enough in energy to form a qubit state, which can be manipulated by EDSR. It can be seen that they are brought close enough together for EDSR at around 4 Tesla. From Fig. 3(b), it is clear that in order for our proposed qubit to operate, the $|\boldsymbol{K},\uparrow\rangle$ state needs to be filled first. In this work, we assume that due to the energy and momentum difference, it will not interact strongly with $|\boldsymbol{K}',\uparrow\rangle$ and $|\boldsymbol{K}',\downarrow\rangle$ states,

Please do not adjust margins

(a) (b)

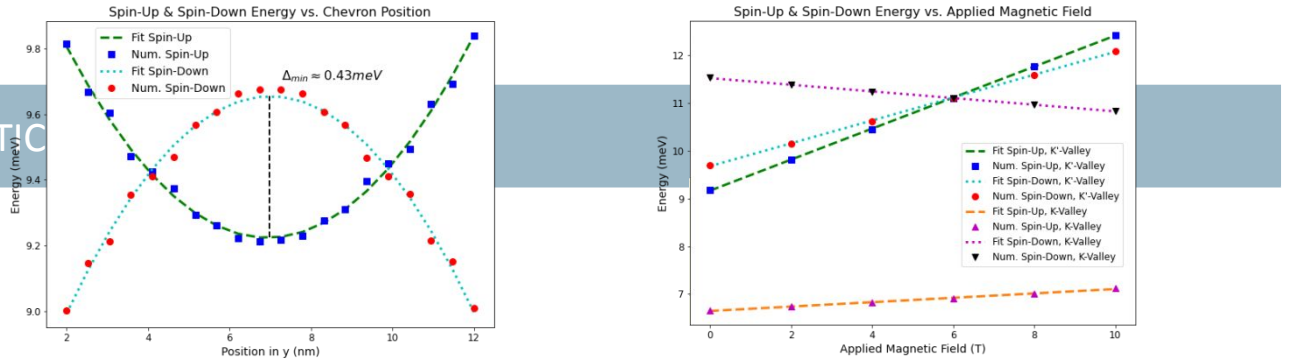

Fig. 3. (a) Calculated energies of spin-up (blue square) and spin-down (red dot) states as a function of the Co NC position in y direction. Dashed and dotted lines are fitting with quadratic equations for the spin-up and spin down states respectively. The black dashed line is positioned where the minimum difference in energy occurs (~7 nm). (b) The energy of the spin-up and spin-down states in the K and K' valleys for different magnetic field strengths. The dashed lines are the linear fits to the numerical results.

and that the effect of the extra charge can be compensated for via the back-gate potential. Future calculations are needed in order to take into account the electron-electron interactions in more detail. Next, the shape of the spin-up and spin-down wavefunctions is

$$E(t) = E_{ac}\cos(\omega_{ac}t)\hat{y} \#(2)$$

studied.

NC-QD Spin-Up and Spin-Down Ground States & Manipulation

The ground states for the spin-up and spin-down electrons are determined by the eigenvectors of the 2D Schrödinger Equation matrix. These are returned in the calculations along with the eigenvalues (energies). Sorting these eigenvectors & eigenvalues, the un-normalized ground states of the NC-QD system are obtained. These un-normalized solutions are integrated and set equal to 1 to determine their normalization factors. Afterwards, the resulting normalized eigenvectors are plotted in Figure 4. In our calculations, we assume that the effect of the magnetic field can be treated separately from that of the NC proximity exchange interaction. In other words, the effect of the magnetic field on the electron in the K'-valley is the same with or without the NC.

This assumption is supported by experimental results,[17] which shows that at magnetic fields below 1 Tesla, a WSe_2/EuS heterostructure experiences strongly enhanced valley splitting on the order of 2.5 meV/T. However, once the applied perpendicular magnetic field exceeded 1 Tesla, the rate of valley splitting with respect to increasing magnetic field returned to that of the WSe_2/SiO_2 system (0.20 meV/T). This lends credibility to our assumption that the magnetic proximity exchange interaction can be treated as position dependent perturbation to the MoS_2 band structure while the effects of external perpendicular magnetic fields remain unchanged.

It is worth noting in Fig. 4 that the spin-down electron state has been squeezed into an egg-like shape due to the influence of the magnetic Co NC. This in turn creates an asymmetry in the y-direction, which results in strong coupling between the spin-up and spin-down states within the NC-QD when coupled with a linear perturbation in the y-direction.

Next, we determine how these electronic states will interact with the time-dependent electric field used for EDSR. The effect of the electric field can be treated as a linear perturbation in the y-direction.[2,20] The electric field has the following form as described in equation (2).

Eqn. 2 describes the magnitude of the electric field in the y-direction versus time, where E_{ac} is the amplitude of the oscillating electric field and ω_{ac} is the driving frequency. In the calculations, t is in nanoseconds. This electric field will perturb the lowest-energy electron (the spin-down ground state $|\mathbf{0},\downarrow\rangle$) from its initial position. Therefore, to determine the form of the time-dependent potential, the initial position of the spin-down electron has to be located, as the perturbing potential relative to its resting position will be measured. Since the potential is asymmetric due to the presence of the NC, the

$$y_{avg} = \langle 0,\downarrow | y | 0,\downarrow\rangle \#(3)$$

average position in the y-direction must be calculated via equation (3).

In equation (3) Bra-Ket notation is used where in general the spin-up and spin-down states are represented by $|\boldsymbol{n},\uparrow\rangle$ and $|\boldsymbol{n},\downarrow\rangle$. In this case 'n' refers to the excitation level of the state and denotes whether the system is spin-up or spin-down. Knowing the equilibrium position, the potential experienced by the spin-down electron due to the perturbing electric field can be calculated. That is the perturbing electric potential that the electron will experience assuming that its initial position defines where the perturbing electrostatic potential is zero. Since the alternating electric field is treated as a perturbation, the above treatment is reasonable as only a relative change in energy due to the electric potential is of interest. The time-dependent perturbing potential is calculated via equation (4).

Please do not adjust margins

$$e^- V_{ac}(t) = e^- E_{ac}\cos(\omega_{ac}t)\langle n \mid (y - y_{avg}) \mid k\rangle \hat{y} = e^- E_{ac}\cos(\omega_{ac}t)\alpha_{nk}\hat{y} \#(4)$$

In equation (4) α_{nk} is a short-hand expression for the overlap between two states in the NC-QD with respect to the linear perturbing potential. Both the left- and right-hand sides of the equation are multiplied by the magnitude of the electron charge, e^-, to convert the time-dependent electric potential into a perturbing energy potential in units of eV. Having determined both the stationary states and the perturbing potential, all that is needed to determine the effect of the applied time-dependent electric field is to plug these results into the perturbative form of the time-dependent Schrodinger equation (5). [21, 22]

$$\frac{d}{dt}c_n = \frac{-i}{\hbar}\sum_k e^- E_{ac}\cos(\omega_{ac}t)\langle n \mid (y - y_{avg}) \mid k\rangle c_k(t) Exp\left[-i(E_k - E_n)t/\hbar\right] \#(5a)$$

$$\frac{d}{dt}c_n = \frac{-i}{\hbar}\sum_k e^- E_{ac}\cos(\omega_{ac}t)\alpha_{nk}c_k(t) Exp\left[-i(E_k - E_n)t/\hbar\right] \#(5b)$$

Equation (5b) generates a series of coupled first order differential equations, which must be solved to determine how the ground state $|0,\downarrow\rangle$ evolves with time under the effect of the time-dependent perturbing potential. In equation (5a), $|n\rangle$ and $|k\rangle$ refer to different stationary states that are calculated previously based on the NC-QD potential. $c_k(t)$ refers to the amplitude of the $|k\rangle$ state at time t with E_k and E_n referring to the previously calculated energies of the $|n\rangle$ and $|k\rangle$ states. The constant electric field term, E_{ac}, and the time-dependent term, $\cos(\omega_{ac}t)$, are factored out since they do not depend on position.

To solve the set of coupled first order ODEs generated by equation (5b), a particular version of the Runge-Kutta method is used, which has been applied to similar resonant perturbation problems in the past.[30,31] The Runge-Kutta algorithm used to solve the system of equations generated by equation (5) comes from SciPy,[27] which uses a 5th order accurate Runge-Kutta method.[32] Next, the electron is assumed to be initially in the ground state and therefore $\boldsymbol{c_0 = 1}$. To make sure that the system considers the possibility of state leakage from the desired lowest energy spin-up and spin-down states, we use the first ten eigenstates of both the spin-up and spin-down NC-QD potential. This give twenty states in total, which are then sorted by energy from lowest to highest, and then are in turn plugged into equation (5) to be solved via the Runge-Kutta method.[32]

One final aspect that needs to be taken care of is the energy splitting between the ground spin-down state ($|\mathbf{0},\downarrow\rangle$) and the ground spin-up state ($|\mathbf{0},\uparrow\rangle$). When a magnetic field is applied in the out-of-plane direction ($+\boldsymbol{B_z}$), the spin-up and spin-down states in the K' valley rise in energy at different rates. Based on the approximately linear change in energy, we can estimate the required magnetic field needed to bring the spin-up and spin-down states close enough in energy for EDSR to occur. In the following, we apply an external magnetic field of 4.75 Tesla on a system with the previously mentioned optimized NC-QD parameters. For these calculations, 158^2 samples of the potential space are used to achieve sufficiently high resolution for the time dependent calculations later. After performing these calculations, the resonant frequency of the resulting system is determined. Equation (6) is used to determine the resonant frequency of a two-state system.

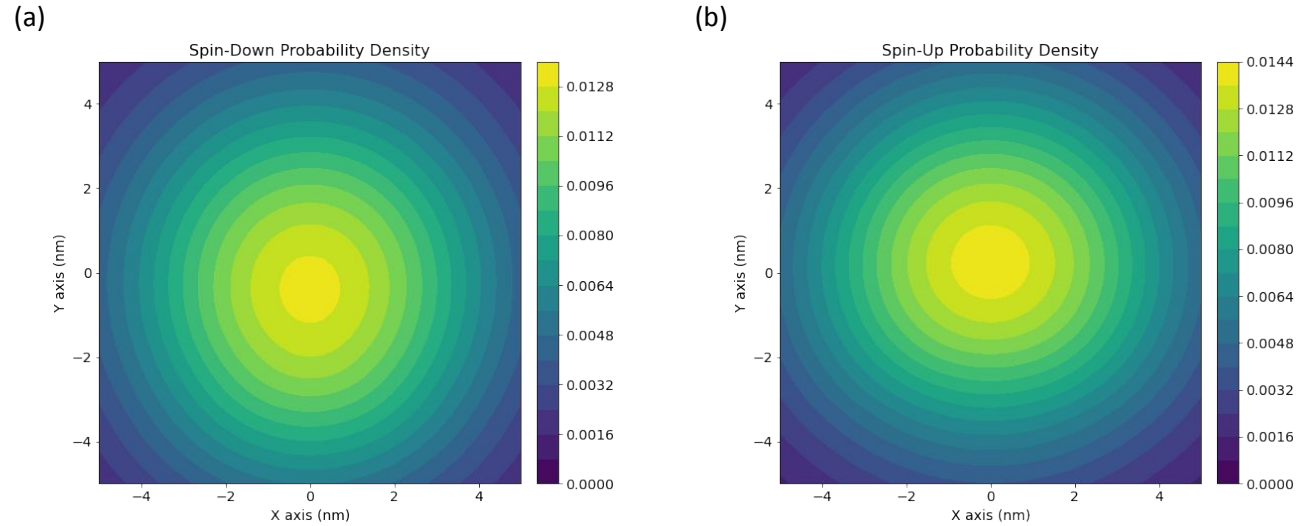

Fig. 4. (a) Normalized probability density of the spin-down electron ground state with a simulation radius of 20 nm. The potential radius is 40 nm and potential depth is 300 meV. (b) Normalized probability density of the spin-up electron ground state in the same system as (a).

This journal is © The Royal Society of Chemistry 20xx

Please do not adjust margins

ARTICLE

$$\omega_0 = \frac{E_{\uparrow,f} - E_{\downarrow,f}}{\hbar},\ \Delta E_f = (E_{\uparrow,f} - E_{\downarrow,f}) = \hbar\omega_0 \#(6)$$

In equation (6), variable $\Delta \boldsymbol{E_f}$ is defined as the difference between the spin-up and spin-down state energies. In our case, the resonant frequency of the system is approximately 20.89 GHz when a 4.75 Tesla magnetic field is applied, which is very similar to the resonant frequency of the state-of-the-art silicon spin qubits (19.7 GHz).[4]

For qubit operations, the π-rotation time or $\boldsymbol{t_\pi}$ is the time it takes for the system to evolve from the spin-down state into the spin-up state with a greater than 0.99 probability, and it is clearly an essential parameter. To calculate this, the 20 lowest states (10 lowest spin-down states and 10 lowest spin-up states) are solved, and then a 5th Runge-Kutta method[27,32] is used to further solve the resulting system of equations generated by equation (5). Doing so, $|\boldsymbol{c_1}|^2$ (the probability of measuring the electron in the lowest energy spin-up state $|\boldsymbol{0},\uparrow\rangle$) is plotted in Figure 5. Since the system is being driven at resonance (20.89 GHz), the value of $\boldsymbol{t_\pi}$ is determined by the amplitude of the perturbing potential, which is the applied electric field. However, to achieve a π-rotation with a high probability, it is necessary to use lower-amplitude electric fields to fulfill the assumptions of the rotating wave approximation (RWA). In this study, the amplitudes of the perturbing electric field are $\boldsymbol{1 \times 10^{-2}\ mV/nm}$, $\boldsymbol{0.75 \times 10^{-2}\ mV/nm}$ and $\boldsymbol{0.5 \times 10^{-2}\ mV/nm}$ for our proposed system, which are in line with the electric field used for the proposed TMDC qubit in reference 33 ($\boldsymbol{1.0 \times 10^{-2}\ mV/nm}$).

It should also be noted that according to the RWA, the value of $\boldsymbol{t_\pi}$is proportional to the magnitude of the driving amplitude. Therefore, larger driving amplitudes will result in smaller $\boldsymbol{t_\pi}$ and vice versa. However, when large driving fields are applied to the system, the transition probability versus time does not behave sinusoidally and therefore $|\boldsymbol{c_1}|^2$ does not predictably approach a value of 1 at these large driving amplitudes. Therefore, smaller driving amplitudes are used to make sure that the transition probability behaves sinusoidally.

The data plotted in Figure 5 is used to determine $\boldsymbol{t_\pi}$ by simply locating the first $|\boldsymbol{c_1}|^2$ maximum. This is done numerically within Python and the location of the maximum is noted in Fig. 5 with a black dashed line for each resonant frequency. The time it takes for $|\boldsymbol{c_1}|^2$ of a given configuration to reach its first maximum is therefore the $\boldsymbol{t_\pi}$ of that particular system.

To keep our results comparable with reported values,[21,23,33-36] we only consider these three driving amplitudes. For the system driven at 0.01 mV/nm, a Rabi frequency of 90.91 MHz is achieved, while Rabi frequencies of 68.49 MHz and 45.45 MHz are obtained for the systems driven at 0.0075 mV/nm and 0.005 mV/nm, respectively. These results are comparable to the proposed defect based MoS_2 QDs,[36] as well as the current silicon based QDs.[3,4]

As observed from Fig. 5, among the three driving amplitudes, only the system driven at 0.01 mV/nm has a rotation time approximately equal to the measured spin-lifetime of MoS_2.[37] However, it is not clear if such measurements are indicative of the spin lifetime of spin-polarized electrons within electrostatic MoS_2 QDs. Up to now, there is a wide range of spin-valley lifetimes reported for MoS_2 and MoS_2 heterostructures, with the heterostructures having reported spin-valley lifetimes of approximately 1000 ns.[38] It is suggested by others that using isotopically defined MoS_2 as well as better substrate isolation could lead to substantially longer spin-lifetimes in MoS_2 QDs, as was accomplished with Si.[39,40] Furthermore, within the proposed NC-QD, the K'-valley and K-valley spin-up and spin-down states are not only separated in terms of energy but also in terms of momentum. This may also increase the qubit lifetime as discussed in reference 36.

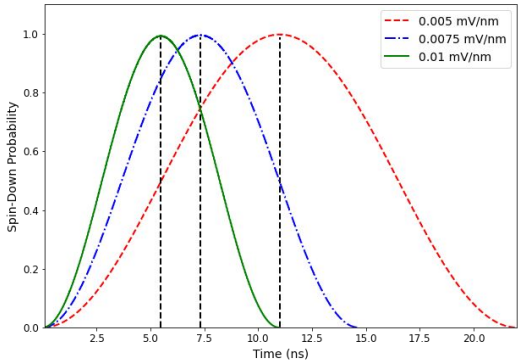

Fig. 5. The green, blue and red curves represent the spin-up probability versus time when a resonant time-dependent potential is applied to the system. The resonant frequency for our proposed system when a 4.75 T magnetic field is applied is approximately 20.89 GHz.

Conclusions

Significant advantages that 2D materials (such as TMDCs) possess in regard to quantum computing have been noticed recently,[39,41] together with other applications of symmetry breaking in 2D layered heterostructures.[42] Furthermore, electrostatically defined TMDC quantum dots have been experimentally demonstrated,[43-47] which indicates that producing electrostatically defined MoS_2 QDs with a 40 nm radius should be feasible.

Please do not adjust margins

The proposed NC-QD takes advantage of the proximity exchange interaction to modify the properties of an MoS_2 electrostatic QD. It should be emphasized that the proposed device is not limited to using Cobalt and in fact many other magnetic materials can be used, provided that the NC is properly optimized and introduces a sufficiently large shift in the spin-up and spin-down energies within the K' valley of the conduction band. Therefore, the design principles behind the proposed device are very general and could be employed to customize the properties of 2D semiconductors via proximity exchange effect in general.

The NC-QD also has several attractive properties from a theoretical perspective, when compared to other proposed MoS_2 QDs. First, the NC-QD does not require either placing or locating a defect for the qubit to operate as is required in reference 36. Second, the NC-QD requires an external magnetic field of much less than 10 Tesla for qubit operation, which is significantly smaller than the 20 Tesla magnetic field required for EDSR as discussed in reference 33 and is therefore much more easily achieved practically. Third, the NC-QD requires gate frequencies of tens of GHz or less for qubit operation as opposed to hundreds of GHz required for spin-valley qubit operation.[21,34] Therefore, the proposed NC-QD design allows for qubit operations to be carried out under more typical experimental conditions, and therefore could be a viable candidate.

Appendix A

The method and rational that we use to decide on an appropriately sized simulation space is presented in this section.

Of primary concern are the lowest energy states of the system, these being the ground states of the electron in the spin-up and spin-down states. Determining the shape and energy of these states is the most important part of our numerical simulation, since these two states determine the resonant frequency of the system as well as the rotation speed. Achieving high resolution of higher energy states is useful for quantifying the amount of leakage that the qubit experiences as it is rotated from spin-down to spin-up. Therefore, we seek to simulate the smallest reasonable space to achieve the highest resolution of the ground states while also minimally changing the shape and energy of the higher energy states.

For a 2D parabolic quantum well represented in x, y coordinates the first 10 states (1 ground and 9 excited) are all contained within the first three excited states. This is because of the combined degeneracy of the first, second and third excited states. Therefore, our goal is to make sure that the dimensions of the simulation space are such that more than 99% of the third excited state wavefunction is captured within the space. To determine the appropriate dimensions, we first define the third excited wavefunction in equations A.1 through A.3.

$$\psi_3(x) = \frac{1}{\sqrt{3}}\left(\frac{m\omega}{\pi\hbar}\right)^{1/4}\left[2x^3\left(\frac{m\omega}{\pi\hbar}\right)^{3/2} - 3x\left(\frac{m\omega}{\pi\hbar}\right)^{1/2}\right]Exp\left[\frac{-x^2 m\omega}{2\hbar}\right]\#(A.1)$$

$$\psi_3(y) = \frac{1}{\sqrt{3}}\left(\frac{m\omega}{\pi\hbar}\right)^{1/4}\left[2y^3\left(\frac{m\omega}{\pi\hbar}\right)^{3/2} - 3y\left(\frac{m\omega}{\pi\hbar}\right)^{1/2}\right]Exp\left[\frac{-y^2 m\omega}{2\hbar}\right]\#(A.2)$$

$$\omega = \sqrt{\frac{k}{m}} = \sqrt{\frac{V_{max}}{mR_{QD}^2}}\#(A.4)$$

$$\frac{m\omega}{\hbar} = \frac{0.44\, m_e}{\hbar}\sqrt{\frac{300\, meV}{(0.44\, m_e)(40\, nm)^2}} \cong 0.0329 nm^{-2}\#(A.5)$$

Although our potential is not a true parabolic potential due to the NC, we consider the standard solutions to be an acceptable approximation. Next, we define $\boldsymbol{\omega}$ and $\boldsymbol{m\omega/\hbar}$ based on chosen QD potential with $\boldsymbol{m = 0.44 m_e}$, $\boldsymbol{R_{QD} = 40nm}$ and $\boldsymbol{V_{max} = 300meV}$ via equations A.4 and A.5.

Next, we sub in our value of $\boldsymbol{m\omega/\hbar}$ and then integrate symmetrically over the x and y coordinates up to finite value α. After this, we solve equation A.6 numerically to determine what value of α is needed to contain more than 99% of $\boldsymbol{\psi_3^*(x,y) \times \psi_3(x,y)}$.

Solving for α numerically we obtain a value of approximately 18.26 nm. Therefore, a simulation limit of 20nm in the positive and negative x, y directions should be adequate for our calculations.

Conflicts of interest

There are no conflicts to declare.

$$0.99 = \int_{-\alpha}^{\alpha}\int_{-\alpha}^{\alpha} \psi_3^*(x,y) \times \psi_3(x,y) dxdy\#(A.6)$$

Acknowledgements

This work was sponsored by the Army Research Office and was accomplished under Grant Number W911NF-19-1-0309.

This journal is © The Royal Society of Chemistry 20xx

References

1. Vandersypen LMK, Eriksson MA. Quantum computing with semiconductor spins. Physics today 2019 Aug;72(8):38-45.
2. Tokura Y, van der Wiel, Wilfred G., Obata T, Tarucha S. Coherent Single Electron Spin Control in a Slanting Zeeman Field. Phys Rev Lett 2006;96(4):047202.
3. Pioro-Ladrière M, Obata T, Tokura Y, Shin Y-, Kubo T, Yoshida K, et al. Electrically driven single-electron spin resonance in a slanting Zeeman field. Nature Physics 2008;4(10):776-779.
4. Watson TF, Philips SGJ, Kawakami E, Ward DR, Scarlino P, Veldhorst M, et al. A programmable two-qubit quantum processor in silicon. Nature 2018;555(7698):633-637.
5. Otsuka T, Nakajima T, Delbecq MR, Amaha S, Yoneda J, Takeda K, et al. Single-electron Spin Resonance in a Quadruple Quantum Dot. Scientific Reports 2016;6(1):31820.
6. Ansaloni F, Chatterjee A, Bohuslavskyi H, Bertrand B, Hutin L, Vinet M, et al. Single-electron operations in a foundry-fabricated array of quantum dots. Nature Communications 2020;11(1):6399.
7. Žutić I, Matos-Abiague A, Scharf B, Dery H, Belashchenko K. Proximitized materials. Materials Today 2019;22:85-107.
8. Zollner K, Faria Junior PE, Fabian J. Proximity exchange effects in MoSe2 and WSe2 heterostructures with CrI3: Twist angle, layer, and gate dependence. Phys Rev B 2019;100(8):085128.
9. Zollner K, Faria Junior PE, Fabian J. Giant proximity exchange and valley splitting in transition metal dichalcogenide/h BN/(Co, Ni) heterostructures. Phys Rev B 2020;101(8):085112.
10. Zhang H, Yang W, Ning Y, Xu X. Abundant valley-polarized states in two-dimensional ferromagnetic van der Waals heterostructures. Phys Rev B 2020;101(20):205404.
11. Henriques JCG, Catarina G, Costa AT, Fernández-Rossier J, Peres NMR. Excitonic magneto-optical Kerr effect in two-dimensional transition metal dichalcogenides induced by spin proximity. Phys Rev B 2020;101(4):045408.
12. Scharf B, Xu G, Matos-Abiague A, Žutić I. Magnetic Proximity Effects in Transition-Metal Dichalcogenides: Converting Excitons. Phys Rev Lett 2017;119(12):127403.
13. Qi J, Li X, Niu Q, Feng J. Giant and tunable valley degeneracy splitting in MoTe2. 2015 Apr 16,.
14. Ciorciaro L, Kroner M, Watanabe K, Taniguchi T, Imamoglu A. Observation of Magnetic Proximity Effect Using Resonant Optical Spectroscopy of an Electrically Tunable MoSe2/CrBr3 Heterostructure. Phys Rev Lett 2020;124(19):197401.
15. Zhong D, Seyler KL, Linpeng X, Wilson NP, Taniguchi T, Watanabe K, et al. Layer-resolved magnetic proximity effect in van der Waals heterostructures. Nature Nanotechnology 2020;15(3):187-191.
16. Norden T, Zhao C, Zhang P, Sabirianov R, Petrou A, Zeng H. Giant valley splitting in monolayer WS2 by magnetic proximity effect. Nature Communications 2019;10(1):4163.
17. Zhao C, Norden T, Zhang P, Zhao P, Cheng Y, Sun F, et al. Enhanced valley splitting in monolayer WSe2 due to magnetic exchange field. Nature Nanotechnology 2017;12(8):757-762.
18. Zhong D, Seyler KL, Linpeng X, Cheng R, Sivadas N, Huang B, et al. Van der Waals engineering of ferromagnetic semiconductor heterostructures for spin and valleytronics. Science advances 2017 May;3(5):e1603113.
19. Thiel L, Wang Z, Tschudin MA, Rohner D, Gutiérrez-Lezama I, Ubrig N, et al. Probing magnetism in 2D materials at the nanoscale with single-spin microscopy. Science 2019;364(6444):973.
20. Pioro-Ladrière M, Obata T, Tokura Y, Shin Y, Kubo T, Yoshida K, et al. Selective Manipulation of Electron Spins with Electric Fields. Prog Theor Phys 2008;176:322-340.
21. Pawłowski J, Żebrowski D, Bednarek S. Valley qubit in a gated MoS2 monolayer quantum dot. Phys Rev B 2018;97(15):155412.
22. Pawłowski J. Spin-valley system in a gated MoS2-monolayer quantum dot. New Journal of Physics 2019;21(12):123029.
23. Kormányos A, Zólyomi V, Drummond ND, Burkard G. Spin-Orbit Coupling, Quantum Dots, and Qubits in Monolayer Transition Metal Dichalcogenides. Physical review. X 2014;4(1):011034.
24. Bieniek M, Szulakowska L, Hawrylak P. Effect of valley, spin, and band nesting on the electronic properties of gated quantum dots in a single layer of transition metal dichalcogenides. Phys Rev B 2020;101(3):035401.
25. Bhuiyan A, Marsiglio F. Landau levels, edge states, and gauge choice in 2D quantum dots. American Journal of Physics 2020;88(11):986-1005.
26. Izaac J, Wang J. Computational quantum mechanics. Cham, Switzerland: Springer; 2018.
27. Virtanen P, Gommers R, Oliphant TE, Haberland M, Reddy T, Cournapeau D, et al. SciPy 1.0: fundamental algorithms for scientific computing in Python. Nature Methods 2020;17(3):261-272.
28. Sudiarta IW, Geldart DJW. Solving the Schrödinger equation for a charged particle in a magnetic field using the finite difference time domain method. Physics Letters A 2008;372(18):3145-3148.
29. Governale M, Ungarelli C. Gauge-invariant grid discretization of the Schr\"odinger equation. Phys Rev B 1998;58(12):7816-7821.
30. Kormann K, Holmgren S, Karlsson HO. Accurate time propagation for the Schrödinger equation with an explicitly time-dependent Hamiltonian. J Chem Phys 2008;128(18):184101.
31. Dahiya B, Prasad V. Dynamics of Particle in a Box in Time Varying Potential Due to Chirped Laser Pulse. Journal of modern physics 2010;1(6):372-378.
32. Dormand JR, Prince PJ. A family of embedded Runge-Kutta formulae. J Comput Appl Math 1980;6(1):19-26.
33. Brooks M, Burkard G. Electric dipole spin resonance of two-dimensional semiconductor spin qubits. Phys Rev B 2020;101(3):035204.
34. Pawłowski J. Spin-valley system in a gated MoS2-monolayer quantum dot. New Journal of Physics 2019;21(12):123029.
35. Brooks M, Burkard G. Spin-degenerate regimes for single quantum dots in transition metal dichalcogenide monolayers. Phys Rev B 2017;95(24):245411.
36. Széchenyi G, Chirolli L, Pályi A. Impurity-assisted electric control of spin-valley qubits in monolayer MoS 2. 2D Materials 2018;5(3):035004.
37. Yang L, Sinitsyn NA, Chen W, Yuan J, Zhang J, Lou J, et al. Long-lived nanosecond spin relaxation and spin coherence of electrons in monolayer MoS_2 and WS_2. Nature Physics 2015;11(10):830-834.

38. Kim J, Jin C, Chen B, Cai H, Zhao T, Lee P, et al. Observation of ultralong valley lifetime in WSe2/MoS2 heterostructures. Sci Adv 2017;3(7):e1700518.
39. Goh KEJ, Bussolotti F, Lau CS, Kotekar-Patil D, Ooi ZE, Chee JY. Back Cover: Toward Valley-Coupled Spin Qubits (Adv. Quantum Technol. 6/2020). Adv Quantum Technol 2020;3(6):2070063.
40. Ye M, Seo H, Galli G. Spin coherence in two-dimensional materials. npj Computational Materials 2019;5(1):44.
41. Liu X, Hersam MC. 2D materials for quantum information science. Nature Reviews Materials 2019;4(10):669-684.
42. Du L, Hasan T, Castellanos-Gomez A, Liu G, Yao Y, Lau CN, et al. Engineering symmetry breaking in 2D layered materials. Nature Reviews Physics 2021.
43. Song X, Liu D, Mosallanejad V, You J, Han T, Chen D, et al. A gate defined quantum dot on the two-dimensional transition metal dichalcogenide semiconductor WSe2. Nanoscale 2015;7(40):16867-16873.
44. Zhang Z, Song X, Luo G, Deng G, Mosallanejad V, Taniguchi T, et al. Electrotunable artificial molecules based on van der Waals heterostructures. Sci Adv 2017;3(10):e1701699.
45. Pisoni R, Lei Z, Back P, Eich M, Overweg H, Lee Y, et al. Gate-tunable quantum dot in a high quality single layer MoS2 van der Waals heterostructure. Appl Phys Lett 2018;112(12):123101.
46. Wang K, De Greve K, Jauregui LA, Sushko A, High A, Zhou Y, et al. Electrical control of charged carriers and excitons in atomically thin materials. Nature Nanotechnology 2018;13(2):128-132.
47. Davari S, Stacy J, Mercado AM, Tull JD, Basnet R, Pandey K, et al. Gate-Defined Accumulation-Mode Quantum Dots in Monolayer and Bilayer WSe2. Phys Rev Applied 2020;13(5):054058.

This journal is © The Royal Society of Chemistry 20xx